thermo

MDPI

Article

A Charge Transport Closure Model for Plasma-Assisted Laminar Diffusion Flames

Sharif Md. Yousuf Bhuiyan [1], Md. Kamrul Hasan [2] and Rajib Mahamud [1,*]

[1] Department of Mechanical, Measurement, and Control Engineering, Idaho State University, Pocatello, ID 83209, USA; sharifmdyousufbhu@isu.edu
[2] Department of Mechanical Engineering, Virginia Military Institute, Lexington, VA 24450, USA; hasanmk@vmi.edu
* Correspondence: rajibmahamud@isu.edu; Tel.: +1-208-282-4399

Abstract

Electrohydrodynamic effects can significantly alter transport processes in reacting flows, even when the plasma is weakly ionized. However, predictive modeling of such plasma–flame interactions remains challenging due to the multiscale coupling among charge transport, fluid motion, and chemical kinetics. This study presents a charge-transport closure model to investigate electrohydrodynamic influences on laminar non-premixed flames. A two-dimensional computational framework in cylindrical coordinates is used to simulate plasma-assisted methane–air diffusion flames under weak electric-field conditions representative of practical combustion environments. To represent plasma–flow coupling in a computationally feasible yet physically consistent manner, a charge-transport formulation based on the drift–diffusion approximation is employed. The model solves transport equations for representative positive and negative charge carriers coupled with Poisson's equation for the electric potential to obtain a self-consistent electric field. This formulation assumes a weakly ionized regime for low-temperature plasma-assisted combustion, in which neutral species dominate the mass and momentum transport, while ionization chemistry is simplified and charge transport primarily influences the flow through electrohydrodynamic body forces and Joule heating. Assuming a weak electric field, the steady flamelet model is applied, in which plasma effects primarily influence scalar transport and local thermal balance rather than inducing significant bulk ionization dynamics. The governing equations are discretized using a high-order compact finite-difference scheme that provides improved resolution of steep gradients in temperature, species concentration, and space-charge density near thin reaction zones. The canonical laminar flame model configuration was validated using the established laminar methane–air diffusion flame benchmark, and steady-state spatial profiles of key transport properties were evaluated. Two-dimensional analysis identified the discharge coupling location as an important factor. The application of discharge in the fuel-air mixing region leads to a clear restructuring of the flame. When the discharge is activated, electrohydrodynamic forcing and ion-driven momentum transfer produce a highly localized, columnar flame with sharp gradients and a confined reaction zone. Compared with the baseline case, the plasma-assisted flame localizes the OH-rich reaction zone, confines the high-temperature region into a narrow column, and enhances downstream H_2O formation.

Keywords: electrohydrodynamic; plasma–flame interaction; diffusion flame; flamelet; electric field

Check for updates

Academic Editors: Peng Yu and Rama Subba Reddy Gorla

Received: 19 January 2026
Revised: 24 March 2026
Accepted: 31 March 2026
Published: 24 April 2026

Copyright: © 2026 by the authors. Licensee MDPI, Basel, Switzerland. This article is an open access article distributed under the terms and conditions of the Creative Commons Attribution (CC BY) license.

1. Introduction

The accurate prediction of flame dynamics in complex flow configurations remains a pivotal challenge in the design and optimization of modern combustion systems, including gas turbines, aero-engine combustors, and next-generation energy conversion devices [1,2]. These systems often operate under conditions in which intricate couplings among fluid dynamics, detailed chemical kinetics, and electrohydrodynamic effects govern performance, stability, and emission characteristics. Plasma-assisted approaches have recently gained attention as active combustion control strategies, which offer a relatively non-intrusive means to influence flame behavior, extend flammability limits, enhance stabilization, and reduce pollutant formation [3,4]. Plasma–flame interaction fundamentally involves the coupling between the applied or self-induced electric field and the limited population of charged species generated by chemi-ionization within the reaction zone [5,6]. Even at a low degree of ionization, the drift and diffusion of these charge carriers can generate electrostatic body forces and localized Joule heating, thereby affecting momentum transport, species transport, and the distribution of heat release [7,8]. These electrohydrodynamic effects may subsequently modify local flow structures and scalar gradients, resulting in observable changes in global flame characteristics, including axial development, stabilization behavior, and liftoff height in laminar diffusion flames [9,10].

Since simulating complex combustion in detail is computationally demanding, simplified models have become essential for practical engineering design. The flamelet concept, originally formalized by Peters [11], has proven particularly powerful for non-premixed combustion. It decouples the detailed chemical kinetics from the flow field by assuming the flame structure resembles that of a one-dimensional laminar flame embedded within the local flow. In this approach, thermo-chemical quantities such as species mass fractions and temperature become unique functions of a few controlling scalars, typically the mixture fraction and a reaction progress variable. This flamelet manifold can be pre-computed and tabulated, offering a substantial reduction in computational expense while retaining a high degree of chemical accuracy [12,13]. The flamelet/progress-variable (FPV) formulation [14] has been successfully extended and validated for a wide range of configurations, including lifted and partially premixed flames [15,16]. The integration of electric field effects into such a framework introduces additional layers of complexity. The electric field couples with the flow through the motion of charged particles. Accurate modeling requires not only a suitable description of the ionization chemistry but also the solution of additional transport equations for charged species and Poisson's equation for the electric potential [17]. Early models, such as those by Hu et al. [18], assumed the electric field stayed constant. This method reduced the feedback of the charge separation on the flow field. More recent works have introduced two-way coupling. For instance, Yamashita et al. [19] solved the Gauss law in simulations of a capillary flame, while Belhi et al. [20,21] incorporated detailed ion transport within a direct numerical simulation (DNS) framework. These studies suggested significant modifications to flame stabilization due to electrostatic forces. However, resolving the full set of ion species transport equations within a detailed chemistry framework remains computationally prohibitive for multi-dimensional design studies. Di Renzo et al. [22] proposed a flamelet progress-variable method tailored for weak electric fields. These scalars are transported with source terms, and mobilities averaged from the underlying detailed ionization mechanism, which is pre-processed and stored within the flamelet manifold. This approach successfully captured the characteristic "diodic" effect, in which flame response differs between positive and negative voltage polarities, and demonstrated the critical role of heavy anions in flame stabilization dynamics.

Conversely, plasma-assisted combustion modeling has advanced along several directions, shaped by the discharge regime, relevant timescales, and primary plasma–flame

coupling mechanisms [23,24]. Early research demonstrated that hydrocarbon flames are inherently weakly ionized due to chemi-ionization processes within the reaction zone [25]. The resulting charged species interact with applied electric fields and generate effects such as charge drift, space-charge phenomena, ionic wind, and Joule heating, even when overall ionization remains low [26,27]. Recent reviews have highlighted the distinction between weakly ionized flame behavior and strongly nonequilibrium plasma-discharge regimes, highlighting the associated modeling challenges [28,29]. Ehn et al. [7] and Nordin-Bates et al. [8] investigated microwave-assisted turbulent flames using a combined experimental and LES framework that incorporated detailed plasma–combustion chemistry while accounting for the effects of the reduced electric field. Their studies demonstrated that non-equilibrium plasma chemistry, particularly singlet oxygen and electron-driven reactions, plays a key role in enhancing flame stability and propagation. Extensive research has examined nonequilibrium plasma chemistry for ignition enhancement and flame stabilization, particularly in pulsed or high-energy discharge environments. In these scenarios, plasma directly affects combustion chemistry by generating radicals and excited species and inducing rapid gas heating, necessitating detailed kinetic models that resolve a broad range of temporal and spatial scales [30–38]. Conversely, under weak electric-field conditions, plasma primarily affects transport processes rather than fundamentally altering chemical pathways. Modeling approaches in this regime typically couple reacting-flow solvers with charged-species transport and electrostatic field calculations, often employing drift–diffusion formulations to capture electrohydrodynamic effects in laminar premixed and diffusion flames [39]. In these configurations, steep scalar gradients, thin reaction zones, and localized electrostatic transport effects demand accurate numerical resolution but do not warrant the computational expense of fully kinetic plasma descriptions. These factors motivate the development of reduced-charge-transport closure frameworks that enable predictive simulation of plasma-assisted laminar diffusion flames with improved computational efficiency.

Accurately modeling combustion requires high spatial accuracy to capture the variations in thermodynamic and electrostatic properties. High-order compact finite difference schemes offer a compelling alternative to traditional second-order methods [40]. These schemes provide excellent spectral resolution with reduced numerical dissipation, which is crucial for capturing instabilities [41–43]. Their application to combustion simulations, however, has been relatively limited. Dobbins and Smooke [44] employed a compact finite difference scheme for unsteady laminar flame calculations, while more recently, Biazar and Mehrlatifan [45] applied it to reaction-convection-diffusion equations. In the context of complex flow geometries, high-order methods are particularly valuable. Haque et al. [46] applied high-order compact finite-difference discretization to flamelet-based scalar transport in laminar flames, where accurate resolution of steep gradients and transport–chemistry coupling is essential. Their results showed that the finite difference scheme provides enhanced spectral-like accuracy while maintaining numerical stability in the presence of strong convective acceleration. The compact finite-difference scheme was further applied to turbulent flame configurations, where it demonstrated improved capability for capturing multiscale interactions among turbulence, scalar transport, and combustion dynamics compared to conventional finite-volume methods [47]. These findings highlight the utility of high-order methods in providing accurate predictions of flame structure and scalar fields. Nevertheless, their applicability to plasma- or electric-field-assisted laminar diffusion flames remains largely unexplored, particularly under conditions involving sharp gradients, space-charge effects, and tightly coupled electrohydrodynamic processes.

Reduced-order approaches suitable for weakly ionized laminar diffusion flames remain limited, especially for configurations in which electrohydrodynamic effects dominate

scalar transport. To address this gap, the present work introduces a closure model for plasma–flame coupling based on a high-order compact finite difference scheme under weak electric-field conditions. The solver is developed in cylindrical coordinates and solves the Navier–Stokes equations coupled with transport equations for positive and negative charged species, along with an electric field solver, and is implemented in Fortran. The fluid dynamics and scalar transport are solved using a fourth-order accurate compact finite difference scheme, extending the methodology validated in [46,47] to ensure sharp resolution of gradients in velocity, species, and electric potential fields. This also included solving transport equations for two representative charge-density scalars and Poisson's equation for the electric potential, with all necessary properties (mobilities, diffusivities, source terms) derived from the ionization mechanism. In plasma-induced flames, the solution contains thin layers in temperature, radical concentration, charge density, and electric potential [48–52]. A lower-order scheme tends to smear these gradients, which weakens the computed electric body force and alters scalar transport. The compact scheme reduces dispersive and diffusive truncation errors while retaining a compact stencil, making it better suited for resolving the coupled flame and electrostatic structure on feasible meshes. Combustion chemistry is efficiently incorporated via a steady flamelet/progress-variable approach, where the thermo-chemical state is retrieved from pre-computed tables parameterized by mixture fraction and progress variable. The proposed high-order compact finite-difference method offers an efficient approach to understanding plasma–flame interactions within the conventional steady flamelet framework.

2. Numerical Model

2.1. Finite Difference Scheme

2.1.1. Governing Equations

The non-dimensionalized compressible Navier–Stokes equations are solved using a fourth-order accurate compact finite difference scheme. The governing equations for mass, momentum, energy, and mixture fraction are formulated in conservative vector form in cylindrical coordinates.

$$\frac{\partial Q}{\partial t} + \frac{\partial A}{\partial Z} + \frac{\partial B}{\partial r} + \frac{1}{r}C = D + E \tag{1}$$

Here, Q denotes the state vector defined in Equation (2). The flux vectors A(=$E^{(1)}$) and B(=$E^{(2)}$) are given in Equation (3), while the source term vectors C and D are specified in Equations (4) and (5), respectively [46,47]. The Navier–Stokes equations are non-dimensionalized using the reference density ρ_{ref}, fuel inflow velocity u_{ref}, reference temperature T_{ref} = 300 K, and channel half height L_{ref}. Pressure and gravitational acceleration are scaled by $\rho_{ref}\ u_{ref}^2$ and $gL_{ref}\ /u_{ref,}^2$ respectively. The Prandtl number (P_r) is set to unity. In the governing equations, the effect of the electric field on charged species transport is introduced through electric drift terms that appear in the convective fluxes. These terms are expressed in non-dimensional form using electric Peclet numbers, where Pe_P and Pe_n denote the electric Péclet numbers for positively and negatively charged species, respectively. Each electric Péclet number is defined as the ratio of the characteristic electric drift velocity to the reference flow velocity, $Pe_{p,n} = K_{p,n}\ E_{ref}/u_{ref}$. The inclusion of Pe_P and Pe_n allows the model to capture the asymmetric response of positive and negative charge carriers to the applied electric field in a physically consistent and computationally tractable manner, which is appropriate for weakly ionized flow conditions.

$$Q = \left[\rho, \rho u, \rho v, \rho e, \rho Z,\ \rho n_P,\ \ \rho n_M\ \right]^T \tag{2}$$

$$A^{(i)} = \begin{bmatrix} pu_i \\ puu_i + p\delta_{1i} - \tau_{1i} \\ pvu_i + p\delta_{2i} - \tau_{2i} \\ u_i(\rho e + p) + u_j\tau_{ij} - q_i \\ pu_iZ \\ \rho n_P(u_i + Pe_PE_i) \\ \rho n_M(u_i + Pe_nE_i) \end{bmatrix} \tag{3}$$

$$C = \begin{bmatrix} pv \\ puv - \tau_{rz} \\ pv^2 - \tau_{rr} \\ v(\rho e + p) - u\tau_{rz} - v\tau_{rr} - q_r \\ r\left(D\frac{\partial\rho}{\partial r}\frac{\partial Z}{\partial r} + \rho\frac{\partial D}{\partial r}\frac{\partial Z}{\partial r} + \rho D\frac{\partial^2 Z}{\partial r^2} + \frac{\rho D}{r}\frac{\partial Z}{\partial r} + D\frac{\partial\rho}{\partial z}\frac{\partial Z}{\partial z} + \rho\frac{\partial D}{\partial z}\frac{\partial Z}{\partial z} + \rho D\frac{\partial^2 Z}{\partial z^2}\right) \\ \rho P(u_i + Pe_PE_i) + \left(\frac{1}{Pe_p}\right) * \left(\rho\frac{\partial^2\rho}{\partial r^2} + \frac{\partial\rho}{\partial r}\frac{\partial Z}{\partial r}\right) \\ \rho P(u_i + Pe_nE_i) + \left(\frac{1}{Pe_{np}}\right) * \left(\rho\frac{\partial^2\rho}{\partial r^2} + \frac{\partial\rho}{\partial r}\frac{\partial Z}{\partial r}\right) \end{bmatrix} \tag{4}$$

$$D = \left[0, 0, g\left(\rho - \rho_{ref}\right), ug\left(\rho - \rho_{ref}\right), -\frac{\rho Z v}{r},\ \rho w_P,\ \ \rho w_M\right]^T \tag{5}$$

$$E = \left[0, 0, \left(\rho - \rho_{ref}\right)E, (q.E), 0, 0,\ 0\right]^T \tag{6}$$

The source terms ρw_P, ρw_M represent the net volumetric production of positive and negative charge carriers due to ionization and recombination processes in the weakly ionized plasma. The source term is modeled as a function of the reduced electric field under a quasi-steady approximation.

The variables u and v denote the streamwise (r-direction) and wall-normal (z-direction) velocity components, respectively. The static pressure is represented by p, ρ denotes the density, e is the total energy, and Z is the mixture fraction. The total energy e is defined as the sum of the internal energy (c_vT) and the kinetic energy $1/2(u^2 + v^2)$. The term $ug\left(\rho - \rho_{ref}\right)$ appearing in H arises from the Boussinesq approximation, with the gravitational acceleration (g) acting in the r-direction [38].

Equations (7) express the stress tensor, with Re and μ being the Reynolds number and the dynamic viscosity, respectively. The density in the model is evaluated using the ideal gas law ($p = \rho RT$), where R is the gas constant.

$$\tau_{zz} = \frac{2\mu}{3Re}\left[2\frac{\partial u}{\partial z} - \frac{\partial v}{\partial r} - \frac{1}{r}\left(\frac{\partial w}{\partial\theta} + v\right)\right],\ \tau_{rr} = \frac{2\mu}{3Re}\left[-\frac{\partial u}{\partial z} + 2\frac{\partial v}{\partial r} - \frac{1}{r}\left(\frac{\partial w}{\partial\theta} + v\right)\right], \quad \tau_{rz} = \frac{\mu}{Re}\left[\frac{\partial u}{\partial r} + \frac{\partial v}{\partial z}\right] \tag{7}$$

The mixture fraction, Z is dependent on the flow velocities (u_i), density (ρ), and mass diffusivity (D). The mass diffusivity for all the species is considered identical ($D_i = D$), and is derived using the relation between mass and thermal diffusion, i.e., Lewis number ($Le == 1$). The mixture fraction ranges from 0 to 1, with 0 being an oxidizer-only flow and 1 being a fuel-only flow.

The wall-normal first derivatives of the Navier–Stokes equations are discretized using fifth-order accurate upwind- and downwind-biased compact finite difference schemes. The viscous terms are evaluated with a fourth-order accurate compact finite difference formulation. The resulting tridiagonal systems are solved using the Thomas algorithm. Temporal integration is performed with a fourth-order Runge–Kutta scheme, where superscripts n

and n + 1 denote consecutive time levels. Further details of the numerical methodology are provided in refs. [46,47].

2.1.2. Electric Field Implementation

The electrostatic potential is governed by the axisymmetric Poisson equation in cylindrical coordinates (r, z), assuming invariance in the azimuthal direction. Under this assumption, the governing equation is written as

$$\frac{1}{r}\frac{\partial}{\partial r}\left(r\,\frac{\partial \varphi}{\partial r}\right)+\frac{\partial^2 \varphi}{\partial z^2}=-\frac{\Delta \rho_e}{\varepsilon_0} \tag{8}$$

Introduce characteristic scales L, φ, ρ for length, potential, and space charge density, respectively, and define the dimensionless variables

$$\widetilde{r}=r/L,\widetilde{z}=z/L,\widetilde{\varphi}=\varphi/\varphi_0,\widetilde{\rho}=\Delta\rho_e/\rho_0 \tag{9}$$

With these definitions, Equation (1) becomes

$$\frac{1}{\widetilde{r}}\frac{\partial}{\partial \widetilde{r}}\left(\widetilde{r}\frac{\partial \widetilde{\varphi}}{\partial \widetilde{r}}\right)+\frac{\partial^2 \widetilde{\varphi}}{\partial \widetilde{z}^2}=-\lambda\widetilde{\rho} \tag{10}$$

where the dimensionless parameter

$$\lambda=\frac{\rho_0 L^2}{\varepsilon_0 \varphi_0} \tag{11}$$

Here, the relative permittivity $\varepsilon_0 = 8.854\times10^{-12}$ F/m, the reference voltage, $\varphi_0 = 1000$, and L is the characteristic length. The parameter λ represents the relative scaling between the charge density and the electric potential in the non-dimensional Poisson equation. It determines the strength of the space-charge term compared to the geometric diffusion of the potential field.

The dimensionless Poisson equation is discretized on a uniform structured grid in the (r, z) plane. Second-order central finite differences are employed for both the radial and axial diffusion terms. The cylindrical geometry is accounted for explicitly in the radial discretization through the 1/r dependence, resulting in asymmetric coefficients for the neighboring radial nodes.

$$r_i = i\,\Delta z\ ,\ i=0,\ \ldots,\ N_r-1$$

$$z_i = j\,\Delta z\ ,\ j=0,\ \ldots,\ N_z-1$$

$$\varphi_{i,j}\approx\varphi\left(r_i,z_j\right)$$

$$\rho_{i,j}\approx\rho\left(r_i,z_j\right)$$

A standard second order finite difference approximation of equation at an interior grid point (i, j) ($2\le i\le N_r-1$, $2\le j\le N_z-1$) yields,

$$A_r{}^{+}\varphi_{i+1,j}+A_r{}^{-}\varphi_{i-1,j}+A_z\left(\varphi_{i,j+1}+\varphi_{i,j-1}\right)-A_0\varphi_{i,j}=-\rho_{i,j} \tag{12}$$

where the (dimensionless) coefficients are

$$A_r{}^{+}=\frac{1}{\Delta r^2}+\frac{1}{2r_i\Delta r}\ ,\ A_r{}^{-}=\frac{1}{\Delta r^2}-\frac{1}{2r_i\Delta r},\ A_z=\frac{1}{\Delta z^2}\ ,\ \ A_0=\frac{2}{\Delta r^2}+\frac{2}{\Delta z^2} \tag{13}$$

Rearranging for $\varphi_{i,j}$, gives the Gauss—Seidel update formula

$$\varphi_{i,j}^{GS} = \frac{\left(A_r{}^{+}\varphi_{i+1,j} + A_r{}^{-}\varphi_{i-1,j} + A_z\left(\varphi_{i,j+1} + \varphi_{i,j-1}\right) - \rho_{i,j}\right)}{A_0} \quad (14)$$

At each interior grid point, the discretized equation couples the potential at the current node to its four nearest neighbors. The resulting algebraic equation preserves second-order accuracy and reflects the geometric effects inherent to cylindrical coordinates. The discrete form is rearranged to yield a pointwise update expression for the electric potential, which is subsequently used in the iterative solution procedure.

The resulting system of linear algebraic equations is solved using a Gauss–Seidel-based successive over-relaxation (SOR) method. The potential is updated sequentially at all interior grid points, while Dirichlet boundary conditions are enforced by prescribing zero potential along all domain boundaries. Convergence is assessed by monitoring the maximum absolute change in the potential field between successive iterations. The iterative process is terminated once the residual falls below a prescribed tolerance.

2.2. Boundary Conditions

Figure 1 illustrates the burner configuration, computational domain, and mesh used in this study. The burner configuration, based on previous experimental studies in the literature [53] for laminar diffusion flame, along with the applied boundary conditions, is shown in Figure 1a,b. The computational grid is non-uniform, with clustering near the walls to better capture steep gradients and boundary-layer effects, as illustrated in Figure 1c.

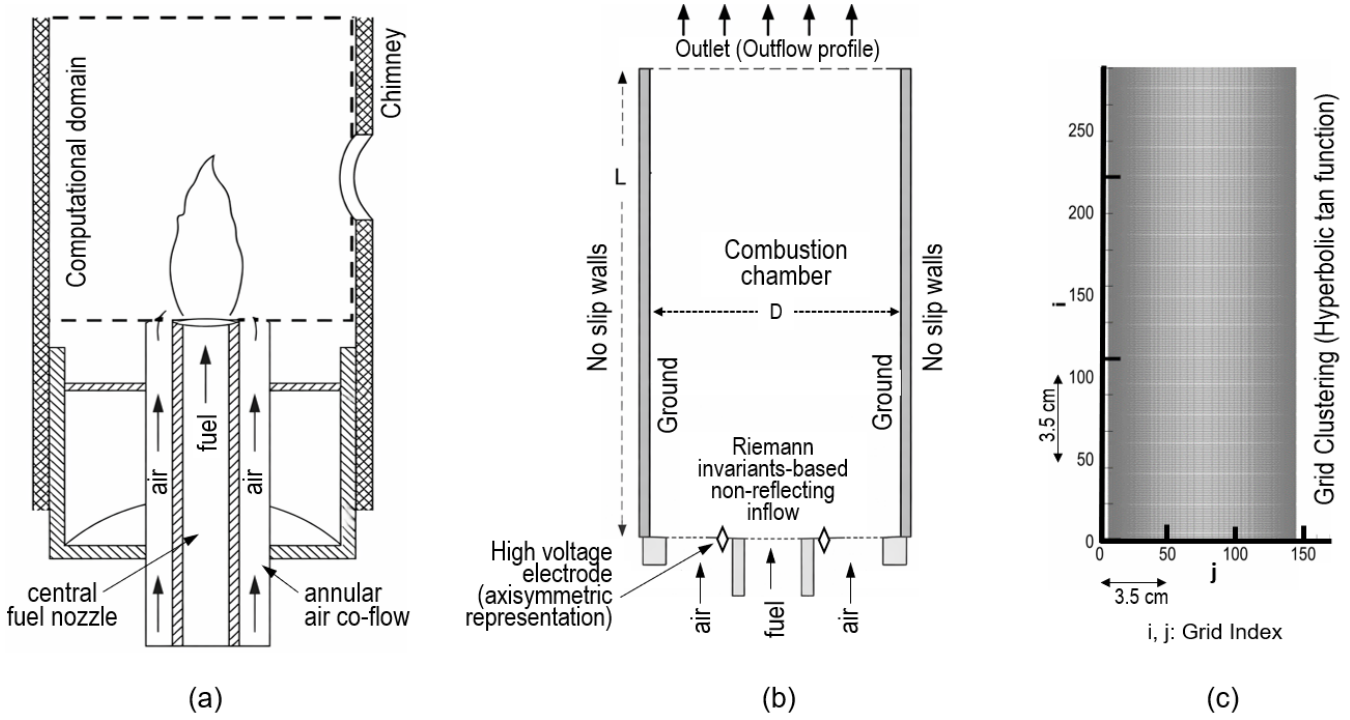


Figure 1. (**a**) Schematic of the burner configuration following the experimental description of the canonical laminar diffusion flame reported in the literature [53]. (**b**) Computational domain and boundary conditions used in the 2D model, including no-slip walls, grounded boundaries, and specified inflow/outflow conditions. (**c**) Non-uniform mesh distribution with grid clustering near the walls to better resolve steep gradients and boundary-layer effects.

The co-flow combustor geometry is based on the experimental investigations of McEnally and Pfefferle [53]. The inner diameter of the fuel inlet (z = 1) is 11.1 mm, which is surrounded by a 0.8 mm thick wall, followed by a concentric annular air inlet (z = 0) of 95.2 mm outer diameter and 3.4 mm thick outer wall. The combustion chamber has a diameter (D) of 102 mm and a length (L) of 200 mm. Fuel and air inlet mass flow rates are specified as 3.608×10^{-6} and 8.65×10^{-4} kg/s, respectively, at 300 K. A no-slip wall is considered for the combustor wall. Inflow (Riemann invariants-based non-reflecting condition) and outflow (characteristics-based) conditions are selected for the inlets and outlet, where the reference profiles are prepared using 1D NS equations (Equation (15)).

$$\frac{\partial p}{\partial x} = \mu \frac{\partial^2 u^*}{\partial y^2}, \ \frac{\partial p}{\partial y} = 0 \ and \ k\frac{\partial^2 T}{\partial y^2} + \mu\left(\frac{\partial u^*}{\partial y}\right)^2 = 0 \quad (15)$$

The developed model solves the cylindrical NS equation, which provides the flexibility to conduct numerical studies on both a 2D planar body and a cylindrical computational domain [44]. Adopting the code to solve for 2D planner domain requires setting the radii to be infinitely long. This minimizes the influence of azimuthal components (θ).

The electric potential is governed by Poisson's equation, and the charge carriers are described using reduced transport equations. The neutral thermo-chemical state is not obtained by solving individual species equations; instead, the only neutral combustion scalar transported in the CFD domain is the mixture fraction, Z. Dirichlet boundary conditions were applied to the electric potential and the ground electrode $\phi = V$ and $\phi = 0$ respectively. For other boundary conditions, Neumann boundary conditions, $\partial\phi/\partial n = 0$, were applied. For the transported mixture fraction, the inlet conditions are prescribed a Z = 1 at the fuel inlet, and Z = 0 at the oxidizer inlet. And at impermeable solid walls and outlet conditions given by $\partial Z/\partial n = 0$ and $\partial Z/\partial x = 0$, respectively.

2.3. Discretization

The governing equations are discretized using a high-order compact finite-difference framework, as discussed in the earlier study [46,47]. The plasma discharge is modeled using a drift–diffusion approximation for positive and negative charge transport, as well as with the Poisson equation for the electric field. The numerical solver, implemented in Fortran, employs a fifth-order scheme for convective transport and a fourth-order scheme for viscous diffusion, which improves the resolution of steep gradients typical of reacting flows. Time discretization is performed using a fourth-order Runge–Kutta method, which has been shown to improve numerical stability and convergence compared to simpler explicit schemes [46]. The present high-order compact finite difference framework is developed for laminar, weakly ionized diffusion flames characterized by steep scalar and electrostatic gradients. The method is particularly suitable for resolving thin reaction zones and charge-density layers with high spatial accuracy.

2.4. Reaction Kinetics

The reaction kinetics in the present study are based on the GRI-type methane–air mechanism, implemented within a steady-flamelet framework to describe a diffusion flame. A limited set of additional reactions relevant to methane flame ionization and charge formation is incorporated. The electron-impact cross-section data and plasma-assisted methane oxidation chemistry are available in the literature from Song et al. and Tennyson et al. [54–56]. Detailed plasma reaction kinetics are not included in the flamelet model, and the plasma effects are represented through a reduced charge-transport formulation under weak electric-field conditions. The source terms for positive and negative ion production are included in the main CFD solver to account for charge generation

and transport. Hence, the model resolves electrohydrodynamic interactions, while strong nonequilibrium discharge physics are not considered. In addition, the steady flamelet assumption (Section 2.5) limits the model's applicability to regimes where the flame structure is primarily determined by mixture-fraction variations, and it does not capture highly unsteady or strongly turbulent combustion dynamics.

2.5. Flamelet Model

The flame dynamics are evaluated using a steady flamelet approach formulated based on a counterflow diffusion flame (Figure 2). In this formulation, the CFD solver transports the mixture fraction z, and the thermochemical quantities required during the solution procedure are obtained from a flamelet table generated from one-dimensional counterflow diffusion-flame calculations in Cantera. The flamelet table is parameterized by mixture fraction over $0 \leq z \leq 1$ and stores temperature, density, species mass fractions, and required transport properties. During the CFD simulation, these quantities are obtained by linear interpolation in mixture fraction space. For post-processing of selected thermochemical fields, a β-PDF reconstruction is applied to smooth and interpret species distributions from the tabulated flamelet manifold. A separate transport equation for the mixture-fraction variance was not solved. Instead, the variance Z'' is calculated in the code algebraically from the local resolved mixture-fraction field. Specifically, it is evaluated based on the deviation of the local mixture-fraction value from its spatially averaged value within the computational domain. The β-PDF is then constructed from the local mean mixture fraction and the prescribed variance, and post-processed quantities such as temperature and species mass fractions are obtained by integration over the flamelet manifold. The details of the flamelet equations and β-PDF integrations are available in the references [11–13,46,47]. The flamelet library is generated using Cantera with a one-dimensional counterflow diffusion flame configuration. The chemical kinetics are described using the GRI-Mech 3.0 mechanism for methane-air combustion. This mechanism includes only neutral species and does not account for ionized species or plasma reactions. Consequently, the generated flamelet table does not contain charged species or electron-related source terms. The present formulation assumes that the applied electric field affects the flow through macroscopic coupling and does not resolve detailed plasma chemistry or ion transport.

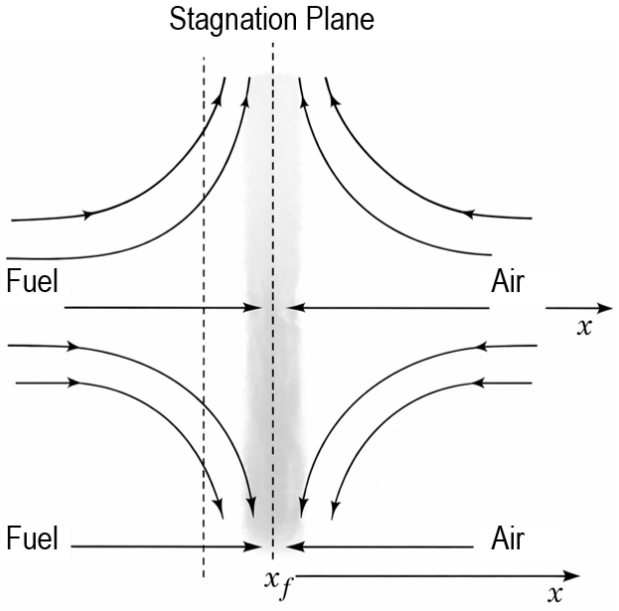


Figure 2. Schematic of the counter-flow diffusion flame used in flamelet generation.

3. Results and Discussion

3.1. Mesh Convergence Analysis

A grid independence study was performed to verify that the numerical solution is independent of mesh resolution and to identify a mesh that provides an appropriate balance between accuracy and computational expense. Four structured meshes were tested for the two-dimensional axisymmetric computational domain: Mesh 1 with 10,368 cells (144 × 72), Mesh 2 with 41,472 cells (288 × 144), Mesh 3 with 165,888 cells (576 × 288), and Mesh 4 with 663,552 cells (1152 × 576).

Figure 3 presents the axial distributions of temperature and mixture fraction predicted using the four mesh resolutions. Clear deviations are observed for Mesh 1 in both profiles, which indicates that the coarsest grid is not sufficient to resolve the main transport and flame structure accurately. For the temperature field, the results from Mesh 2, Mesh 3, and Mesh 4 are in close agreement over the full axial distance, including the rapid rise region, the peak temperature zone, and the downstream decay. For the mixture fraction profile, Mesh 2 shows noticeable improvement over Mesh 1 and follows the same overall trend as the finer meshes, while Mesh 3 and Mesh 4 exhibit only minor additional changes. These results show that the solution becomes weakly sensitive to further grid refinement beyond Mesh 2, particularly for the temperature distribution, which is the main parameter of interest in the present study. Although Mesh 3 and Mesh 4 provide slightly finer resolution in the mixture fraction field, the improvement is limited relative to the substantial increase in cell count and computational cost. On this basis, Mesh 2 was selected for all simulations, since it provides accurate predictions with efficient use of computational resources.

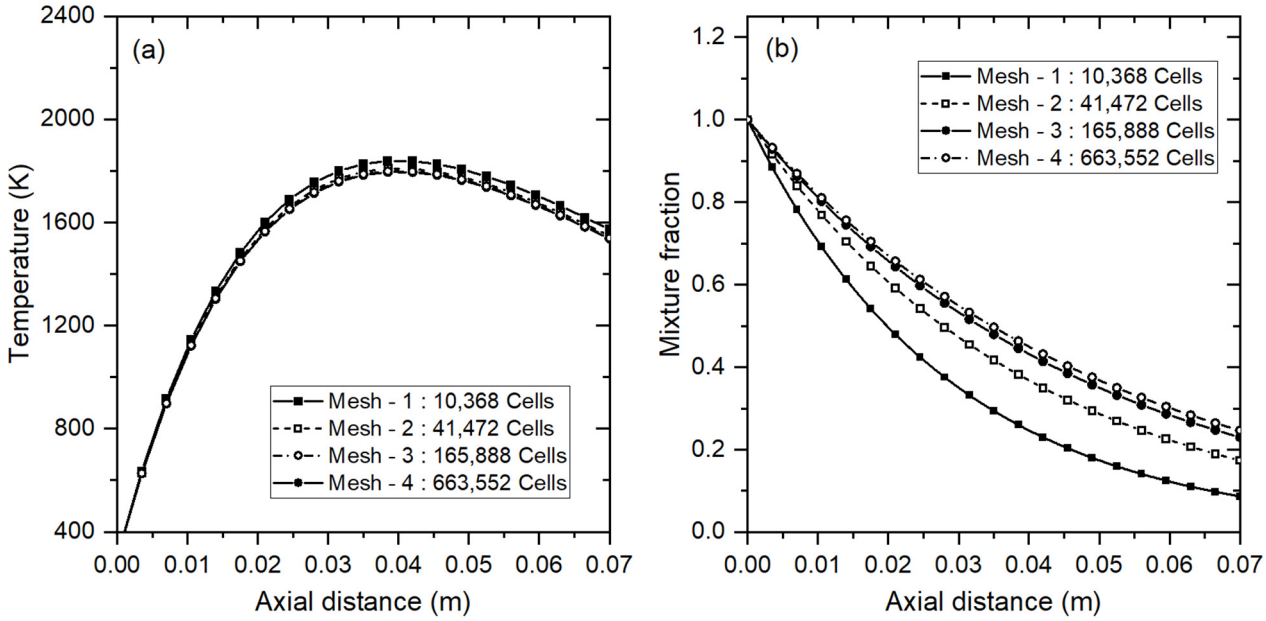


Figure 3. Comparison of axial temperature (**a**) and mixture fraction (**b**) distributions for the two-dimensional non-premixed laminar methane–air flame obtained with four mesh resolutions.

3.2. Model Validation

The present model predictions are compared with both the experimental measurements and the numerical results of Smooke et al. [57], as shown in Figures 4 and 5 for the baseline case. Figure 4 compares radial temperature profiles at axial locations z = 1 cm and z = 1.5 cm, plotted along the radial direction from the centerline (r = 0). The comparison is conducted at the same Reynolds number, with identical fuel and air inlet diameters and volumetric flow rates for the laminar diffusion flame. The burner consists of a 12 mm

diameter vertical fuel tube, with the oxidizer flowing through the annular region between this tube and a 102 mm diameter concentric outer tube. The inlet conditions follow those reported in the literature, with the oxidizer (air) supplied at 40,000 cm^3/min and the fuel consisting of methane (240 cm^3/min).

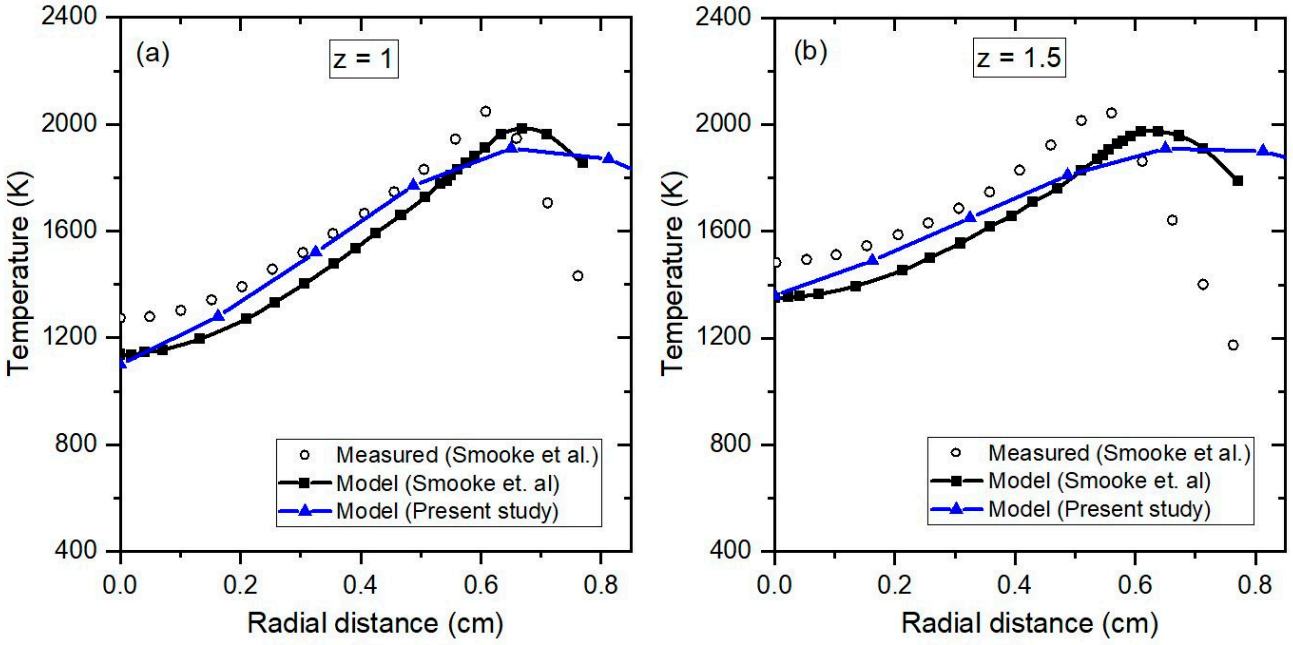


Figure 4. Radial temperature profiles at axial locations (**a**) z = 1 cm and (**b**) z = 1.5 cm for a laminar methane-air coflow diffusion flame: comparison of present model predictions with experimental data and Smooke et al. [57] simulations.

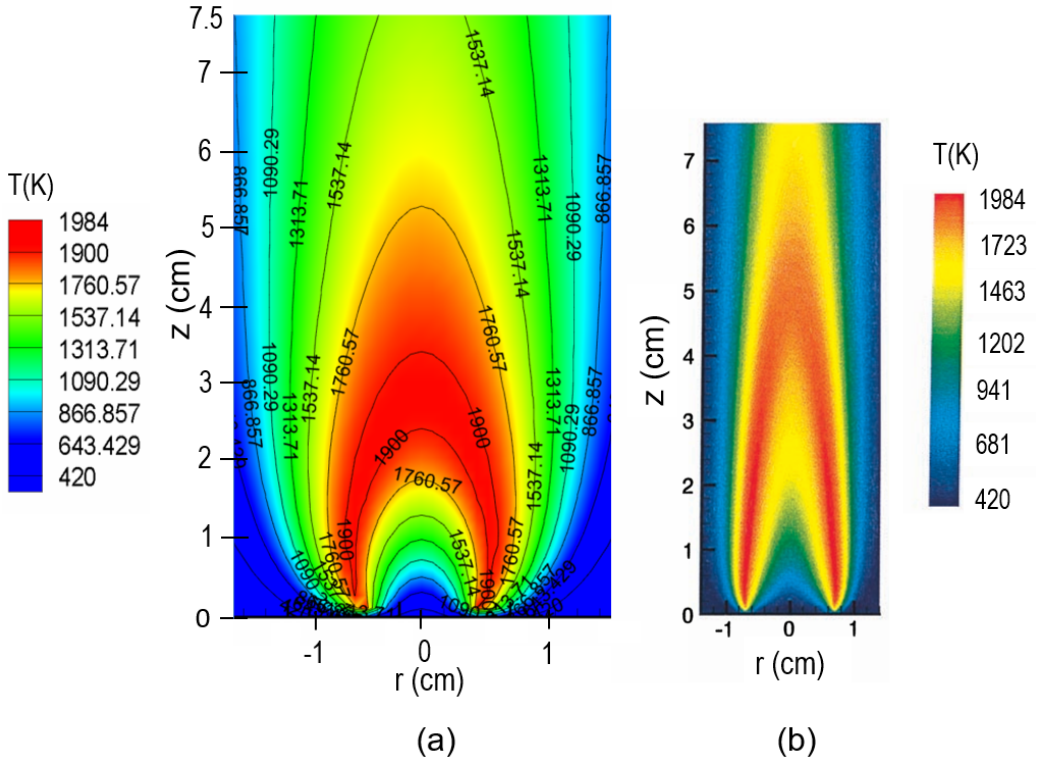


Figure 5. Comparison of two-dimensional temperature distributions: (**a**) present model and (**b**) Smooke et al. [57], showing radial–axial variation and peak flame structure.

The flame configuration consists of a confined, axisymmetric co-flow system at atmospheric pressure, where a central methane jet issues into an annular air stream. Based on the fuel inlet conditions, the flow remains in the laminar regime, with a characteristic fuel-jet Reynolds number of Re $\approx$ 25 defined based on the fuel jet diameter and inlet velocity. At both axial positions, the model captures the overall radial distribution of temperature, including the increase from the centerline toward the flame zone and the peak temperature location in the reaction region. However, some deviations are observed compared to the experimental results. The present model slightly underpredicts the peak temperature and shows a smoother radial gradient compared to the measurements. The deviation is more pronounced on the fuel-rich side near the centerline, where temperatures are lower than the experimental data. This trend is consistent with previous numerical studies, where centerline temperatures are often underpredicted due to boundary conditions and transport–chemistry coupling. Additionally, simulations reported in the literature [57] included detailed transport modeling and finite-rate chemical kinetics, which may explain the improved agreement with experimental peak values. Therefore, the observed differences are likely due to the use of a steady-flamelet formulation in the present model, which provides computational efficiency but may not fully capture the sharp gradients resolved by simulations with detailed transport and finite-rate chemistry.

In addition to comparing temperature, the spatial temperature contours in Figure 5 also compare the present model with the study of Smooke et al. [57]. The predicted flame shows the typical elongated diffusion flame shape, with a clear high-temperature core and a gradual drop in temperature both outward and upward. The peak temperature location, flame height, and spreading are consistent with the results of Smooke et al. This match suggests that the solver captures the main effects of convective transport, molecular diffusion, and chemical heat release that shape the thermal structure of laminar non-premixed flames. However, the model validation presented in this study is limited to baseline cases without an applied electric field. This validation confirms the accuracy of the flow solver and flamelet-progress variable approach. The electric field is incorporated through additional coupling terms, and its implementation is based on established electrohydrodynamic formulations. However, no direct validation against experimental data on electric-field or plasma effects is performed in the present work. Therefore, the results under electric-field conditions should be interpreted as a first-order assessment of the electrohydrodynamic influence on the flame, rather than as a fully validated prediction of plasma-assisted combustion. The parametric study of weak electric-field plasma effects was conducted using the experimental configuration reported by McEnally and Pfefferle [53], which had been validated [46].

3.3. Flow Field Analysis

Figure 6 presents the spatial distribution of normalized electric potential, along with the radial and axial electric field components predicted by the drift–diffusion solver for the baseline laminar diffusion flame. The electric potential changes smoothly across the domain, but sharper gradients appear near the burner exit, where space-charge density is highest. These local distortions are caused by the buildup of charged species in the thin reaction zones, which create weak but noticeable electric-field structures.

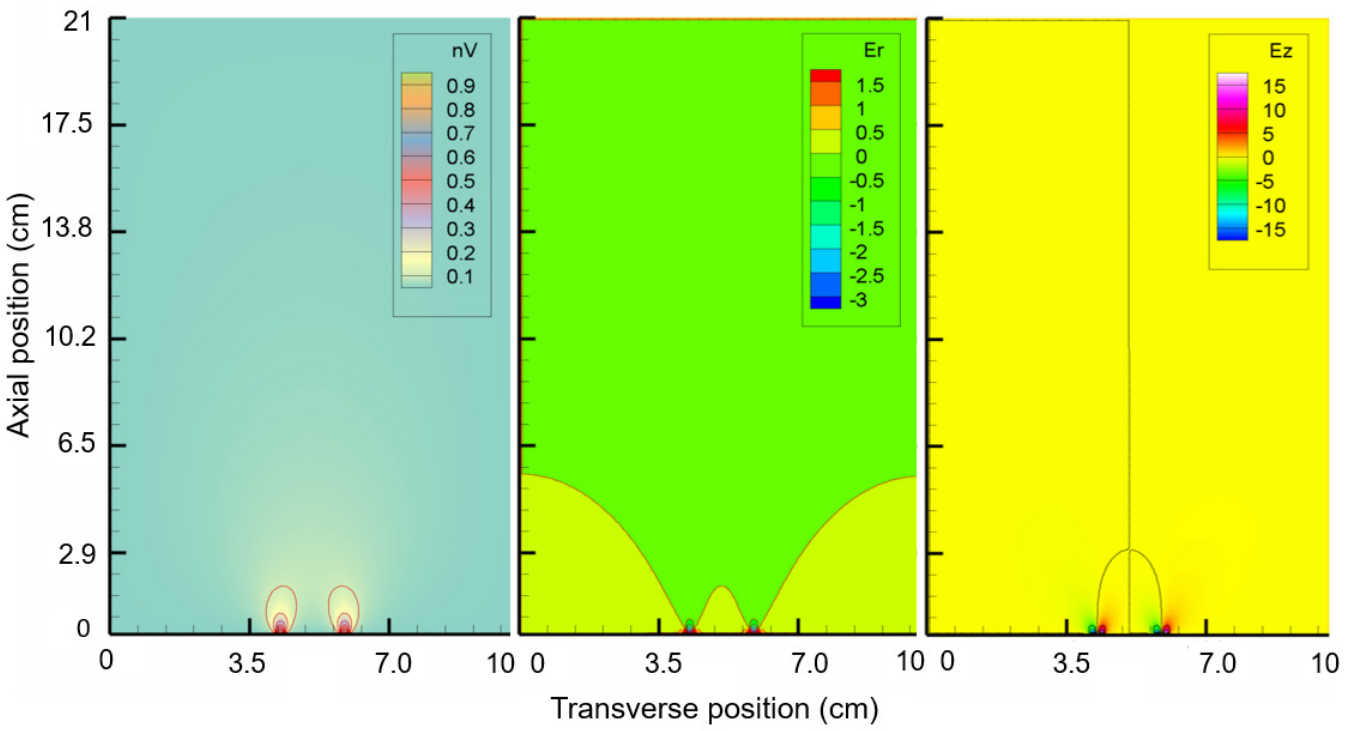


Figure 6. Spatial distribution of normalized electric potential and electric field components (radial E_r and axial E_z) obtained from the drift–diffusion formulation under plasma discharge conditions. The normalized potential (nV) is scaled by a reference voltage of 1000 V, while Er and Ez are normalized accordingly.

The radial electric field component, Er, remains relatively weak across the domain and is predominantly localized near the flame base and within the shear layer due to the applied high voltage in this region. This pattern matches the predominantly axisymmetric charge distribution imposed by the boundary conditions and shows that radial electrohydrodynamic forces are confined to narrow regions with strong charge-density gradients. On the other hand, the axial electric field component, Ez, varies more near the electrode and flame stabilization region, where the potential gradients are strongest. The direction and strength of the axial field depend on the boundary potential and how charge carriers are redistributed, as predicted by the drift–diffusion model. These results show that even under weakly ionized conditions, the interaction between electric potential gradients and charge motion creates local electric-field structures that can affect momentum transport and mixing in the downstream flame. The stronger axial electric field suggests that electrohydrodynamic effects mainly change the axial flow, while radial effects are less important and stay close to the reaction zone. Figures 7–12 present a comparative visualization of the baseline case (left side of each panel, discharge off, i.e., no plasma forcing) and the plasma-forced case (right side of each panel, discharge on) for temperature, mixture fraction (Z), OH radical distribution, and H_2O mass fraction. These results correspond to the burner configuration used in the experimental study of McEnally and Pfefferle [53] and the numerical study of Haque et al. [46]. The burner consists of a central fuel jet (inner diameter $\approx$ 11.1 mm) surrounded by a concentric annular air stream within a 102 mm diameter, 200 mm long combustion chamber. Fuel and air mass flow rates are 3.61×10^{-6} kg/s and 8.65×10^{-4} kg/s, respectively, with inlet conditions specified at 300 K.

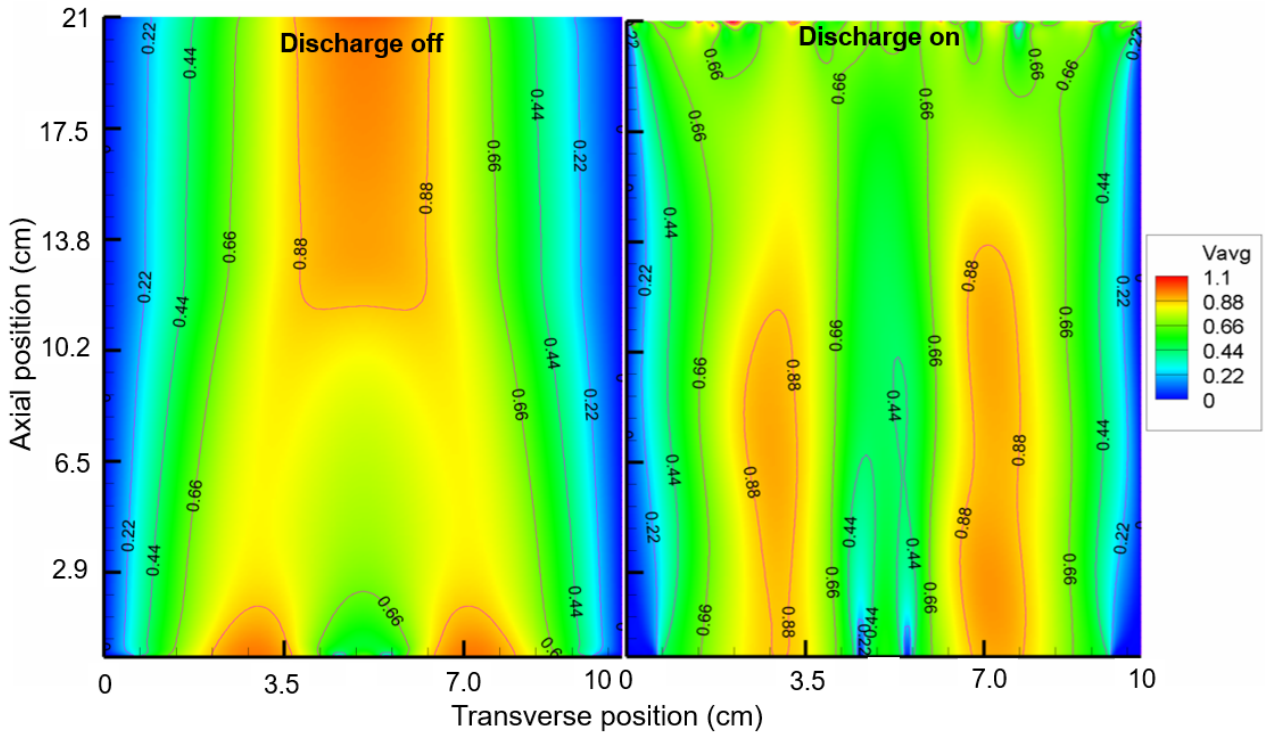


Figure 7. Influence of electric-field-induced transport on diffusion flame structure predicted using a high-order scheme. The dimensionless velocity V_{avg} is normalized to the air-jet velocity (49 m/s) [46].

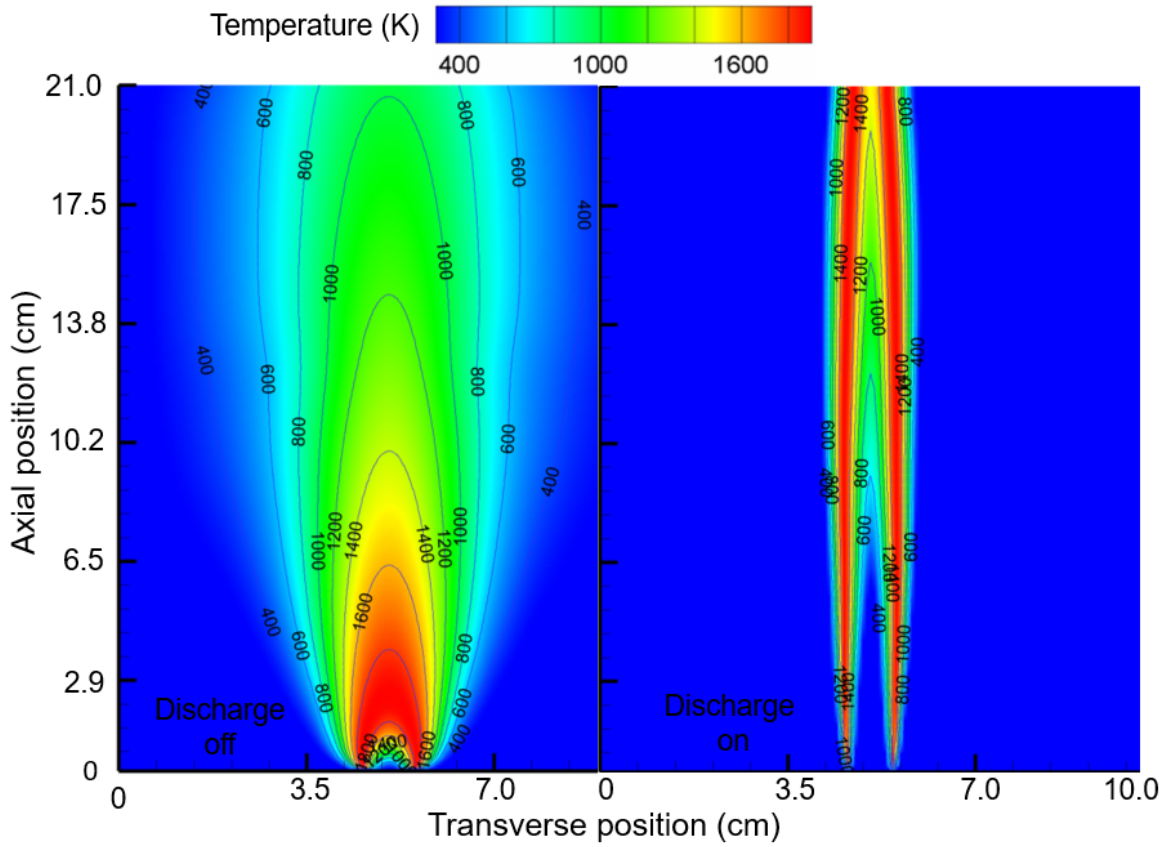


Figure 8. Contours of Temperature (T) in the r–x plane comparing the baseline case without plasma forcing (**left**) and the plasma-forced case (**right**). Plasma forcing significantly modifies the spatial distribution of temperature, leading to a narrow, columnar high-temperature region with enhanced axial persistence.

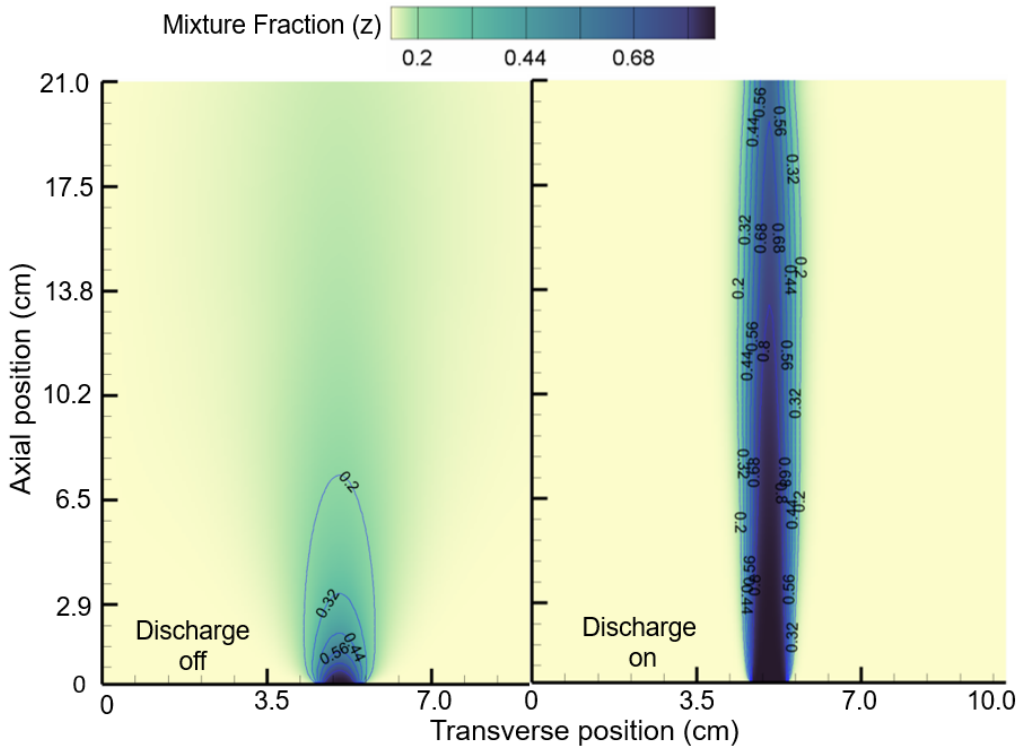


Figure 9. Mixture fraction contours in the r–z plane for baseline (discharge off) and plasma-forced (discharge on) cases, highlighting plasma-induced modifications to flame structure and axial temperature distribution.

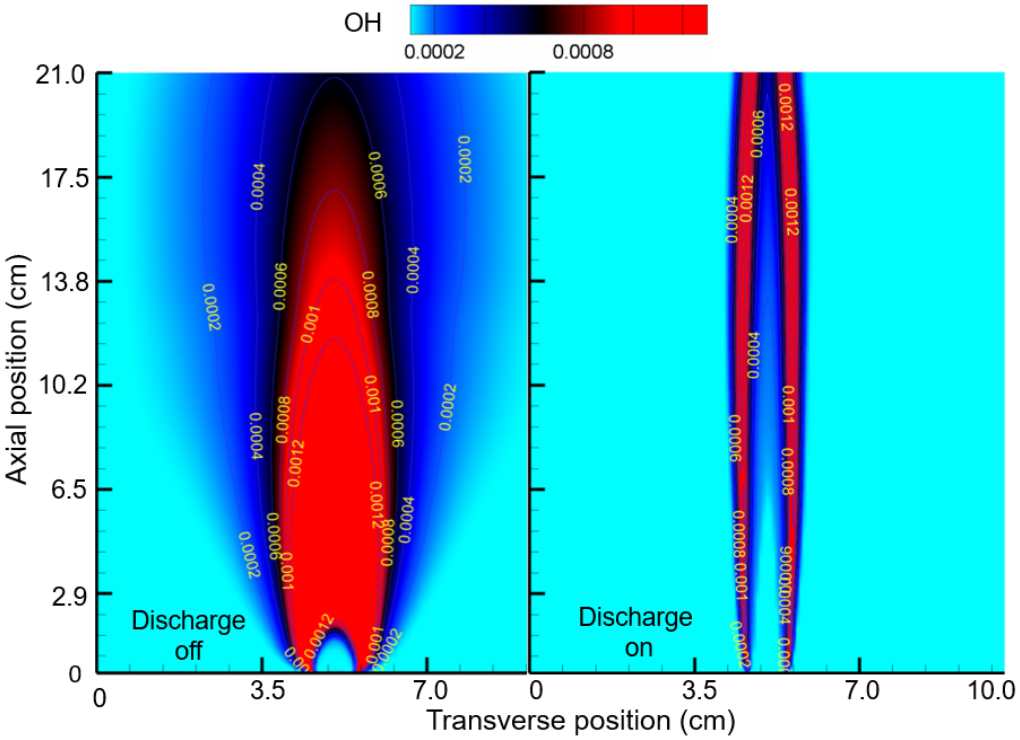


Figure 10. Contours of OH mass fraction in the *r*–*x* plane comparing the baseline case without plasma forcing (**left**) and the plasma-forced case (**right**). Plasma forcing significantly modifies the spatial distribution and persistence of OH radicals, indicating enhanced and sustained chemical activity near the jet core and along the axial direction.

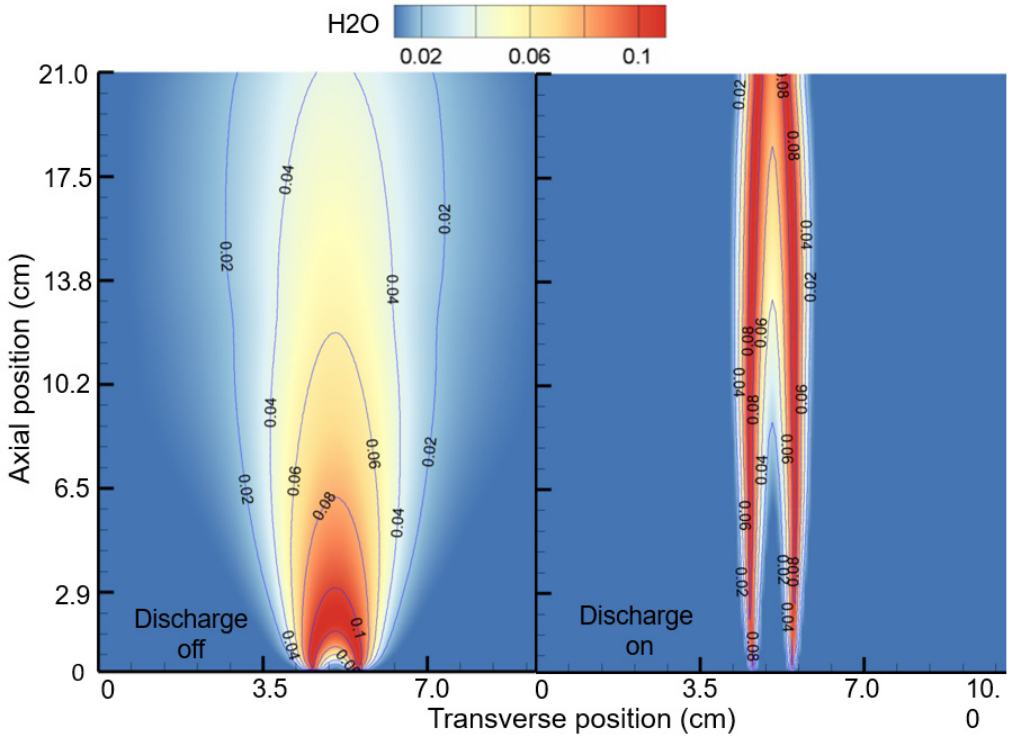


Figure 11. Contours of H_2O mass fraction in the r–z plane for the baseline (discharge off) and plasma-forced (discharge on) cases, illustrating the effect of plasma forcing on product species distribution and axial flame structure.

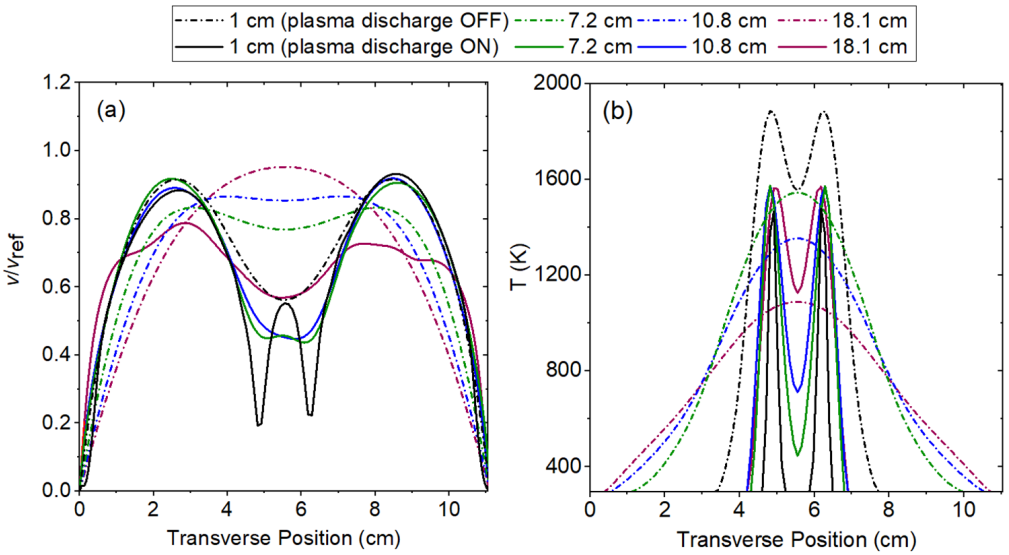


Figure 12. Radial profiles at selected axial locations under plasma-off and plasma-on conditions: (**a**) normalized velocity; (**b**) temperature.

Figure 7 compares the spatial distribution of the velocity magnitude in the flame region between cases with and without plasma discharge. In the baseline condition (discharge off), the flow field exhibits a relatively diffusive profile, characterized by gradual jet spreading and a progressive reduction in peak velocity as the flow progresses downstream. The high-velocity core remains confined near the centerline in the upstream region, while further downstream the contours indicate enhanced radial diffusion and momentum loss due to viscous effects and entrainment of the surrounding coflow. When the plasma discharge is activated, noticeable modifications in the flow structure emerge. The velocity field shows

localized regions of higher magnitude, particularly in the mid- and downstream sections of the domain. These regions correspond to zones where the electric field interacts with the flow field and generates electrohydrodynamic forcing that introduces additional axial momentum into the flow. As a result, the decay of velocity along the streamwise direction is reduced, and the flow maintains stronger convective transport over a larger portion of the flame length.

Plasma forcing significantly modifies the jet topology, leading to enhanced flow localization and the formation of structured high-velocity regions. Unlike the baseline case, the discharge introduces pronounced flow focusing and spatial non-uniformity driven by electrohydrodynamic forces. This indicates that, even under weakly ionized conditions, the plasma acts not only as a momentum enhancement mechanism but also as a driver of flow reorganization at the local scale. The strengthened convective motion observed in the discharge case is consistent with trends in the scalar fields discussed in the following section, including the downstream extension of the high-temperature region and the sustained presence of reactive intermediates. These coupled effects suggest that electrohydrodynamic forcing influences flame transport processes by altering residence time, mixing characteristics, and the spatial structure of the reaction zone in laminar diffusion flames.

In addition, the temperature field exhibits a pronounced transition from a relatively broad distribution in the baseline case to a narrow, columnar structure under plasma forcing (Figure 8). This indicates reduced radial spreading and enhanced axial persistence of the high-temperature region. Such behavior is consistent with the previously observed flow acceleration (Figure 7), where electrohydrodynamic forcing enhances convective transport along the jet axis. As a result, thermal energy is more effectively advected downstream, leading to sustained high temperatures and a more localized reaction zone. These coupled effects suggest that plasma forcing not only adds energy through Joule heating but also redistributes it by modifying the convective transport processes within the flame.

The influence of plasma forcing on scalar transport is evident from the mixture fraction (z) contours (Figure 9). Without plasma forcing, the z field shows a relatively diffusive axial decay with limited radial spreading, reflecting mixing dominated by the underlying flow field. In contrast, the plasma-forced case exhibits a redistribution of Z near the core region, with altered gradients and enhanced axial dispersion. This formation indicates that plasma forcing modifies scalar transport by altering the mixture-fraction distribution and gradient structure via electrohydrodynamic body forces. The observed changes in scalar distribution are attributed to electrohydrodynamic body forces that modify convective transport.

In the absence of the electric field (baseline case), the OH contours exhibit a relatively broad reaction zone originating near the jet base and extending downstream with gradual radial spreading (Figure 10). This behavior is characteristic of a diffusion-controlled flame, where the reaction zone is governed by thermal and molecular transport processes. The OH concentration gradually decreases along the axial direction, indicating a reduction in reaction intensity as reactants are consumed and mixing with the surrounding oxidizer increases. With plasma forcing, the OH field undergoes a pronounced transformation in both spatial distribution and persistence. The reaction zone becomes highly localized, forming a narrow, columnar structure with strong confinement near the centerline and significantly reduced radial spreading. In addition, the OH-rich region persists farther downstream compared to the baseline case. This formation indicates that plasma forcing enhances radical production and sustains active chemistry over an extended axial region. The observed localization and persistence are consistent with plasma-assisted pathways that promote the generation of reactive species and reinforce the reaction zone beyond what is achieved through purely thermal processes.

The H_2O contours illustrate the combined effect of plasma forcing on product formation and transport (Figure 11). In the baseline scenario, H_2O accumulates gradually downstream of the reaction zone, resulting in a broad spatial distribution due to diffusion and mixing. When plasma forcing is applied, the H_2O-rich region becomes more confined and extends further along the axial direction, which aligns with the localized temperature and OH concentration fields. This observation demonstrates that enhanced convective transport and sustained reaction activity promote increased product formation and persistence downstream. These findings indicate that plasma forcing affects not only local heat release and radical production but also alters scalar transport, producing a more localized and extended product distribution along the jet axis.

Figure 12 presents radial profiles of velocity and temperature at selected axial locations for both plasma-off and plasma-on cases, and illustrates the influence of plasma forcing on the flow and thermal fields. The velocity profiles show a clear double-peak structure, which originates from the shear layers between the central fuel jet and the surrounding co-flow. In the absence of plasma, the velocity magnitude decreases progressively with axial distance. This behavior results from viscous diffusion and flow development, which redistribute momentum and produce a flatter profile downstream. When plasma is applied, the velocity field changes significantly. Higher velocity levels are sustained, especially at downstream locations. This behavior is driven by the electrohydrodynamic body force generated by the electric field, which accelerates the flow in regions of charge accumulation, primarily along the shear layers and reaction zone. As a result, the natural decay of velocity is partially suppressed, and momentum is maintained farther downstream. This modification of the velocity field directly impacts transport processes. The enhanced flow strengthens convective transport of heat and species, which supports the extension of the reaction zone and sustains chemical activity downstream. Near the inlet, the effect of plasma remains limited because the flow is controlled by the inlet boundary conditions. However, its influence becomes increasingly pronounced with axial distance as electrohydrodynamic effects accumulate.

The temperature profiles show a clear transition in flame structure under plasma forcing. In the baseline case, the temperature rises from the ambient level and remains relatively broad in the radial direction, indicating a distributed reaction zone governed by mixing and diffusion. As the flow develops downstream, the thermal field spreads further, reflecting gradual heat release over a wider region. With plasma forcing, the temperature profiles become much more localized, exhibiting sharper peaks and steeper radial gradients. A pronounced double-peak structure appears, indicating that the strongest heat release is concentrated within the shear-layer reaction zones, while the centerline remains comparatively cooler. This behavior is consistent with plasma-induced electrohydrodynamic transport, which modifies mixing and convective transport and confines the reaction zone to a narrower region. Farther downstream, the plasma-forced case continues to maintain a more localized thermal structure with reduced radial spreading, indicating sustained reaction activity and stronger thermal confinement compared to the baseline case.

4. Conclusions

A high-order numerical framework was developed to investigate plasma-assisted transport phenomena in laminar methane–air diffusion flames under weak electric-field conditions. The charge-transport closure model enables computationally efficient representation of plasma–flow–chemistry coupling in a weakly ionized reacting environment. The transport equations for positive and negative charges were solved using the drift–diffusion approximation and coupled with Poisson's equation to obtain a self-consistent electric field. This reduced formulation allows plasma effects to influence the reacting flow primar-

ily through electrohydrodynamic body forces and Joule heating. A high-order compact finite-difference scheme combined with explicit Runge–Kutta time integration is used to accurately capture sharp gradients in temperature, mixture fraction, and space-charge density near thin reaction zones. The baseline laminar diffusion flame was validated against the canonical Smooke laminar methane–air diffusion flame in terms of temperature–mixture fraction behavior and major reactive scalar distributions. Plasma-assisted simulations indicated that even in weakly ionized regimes typical of low-temperature plasma-assisted combustion, charge transport produces measurable electrohydrodynamic modifications of the reacting flow. The plasma-induced electric field enhances downstream convective transport by partially counteracting viscous momentum decay, thereby extending the high-temperature region and prolonging the OH-rich reaction zone. Increased downstream H_2O accumulation further demonstrates that plasma-induced transport alters the local thermal balance and the evolution of the reactive scalar.

The proposed model is well-suited for resolving laminar flame structures and weakly ionized plasma–flow interactions under moderate electric-field conditions. Owing to the high resolution provided by the compact finite-difference formulation, the method can effectively capture strong spatial gradients in velocity, temperature, and species fields. This capability makes the approach particularly useful for parametric investigations of electric-field effects on flame structure and transport in simplified configurations. However, the present formulation is restricted to structured meshes and its applicability to complex geometries, strong plasma forcing, and highly nonequilibrium discharge conditions remains to be fully established. The model is developed for weakly ionized, laminar, two-dimensional diffusion flames and does not incorporate detailed plasma chemistry or strongly nonequilibrium discharge physics. Combustion is represented through a steady flamelet approach, which limits its direct applicability to highly unsteady or turbulence-dominated regimes. Furthermore, validation is currently limited to baseline cases without electric-field forcing; therefore, the plasma-assisted predictions should be interpreted as indicative rather than fully validated. Additional simplifications are introduced in the treatment of species transport and electrostatic boundary conditions, and the electric potential equation is discretized using a lower-order scheme compared to the high-order flow solver. Accordingly, the results should be interpreted in light of these assumptions, particularly when applying the model to more realistic or complex plasma–combustion scenarios.

Author Contributions: Methodology: S.M.Y.B., M.K.H. and R.M.; Formal Analysis: S.M.Y.B., M.K.H. and R.M.; Validation: S.M.Y.B., M.K.H. and R.M.; Writing—Original draft: S.M.Y.B.; Writing—review and editing: R.M.; Conceptualization: R.M.; Supervision: R.M. All authors have read and agreed to the published version of the manuscript.

Funding: The work was supported by the internal grant of Idaho State University.

Data Availability Statement: The datasets generated and/or analyzed during the current study are available from the corresponding author on reasonable request.

Conflicts of Interest: The authors declare no conflict of interest.

Nomenclature

A, B	Flux vectors in r and z directions
C, D	Source term vectors
C	Model constant for mixture fraction variance
D	Combustor diameter, m
Di	Inner diameter of fuel inlet, m
e	Total energy per unit mass, J kg^{-1}

E	Electric field, V m^{-1}
f	Body force per unit volume, N m^{-3}
Fr	Froude number
H	Energy flux term
L	Combustor length, m
N	Number of grid points in flamelet table
p	Pressure, Pa
Pe_p	Electric Péclet number for positive charge
Pe_n	Electric Péclet number for negative charge
Q	State vector of conserved variables
Re	Reynolds number
R	Gas constant, J kg^{-1} K^{-1}
r	Radial coordinate, m
T	Temperature, K
u	Velocity in radial direction, m s^{-1}
v	Velocity in axial direction, m s^{-1}
v_{air}	Air inlet velocity, m s^{-1}
v_{fuel}	Fuel inlet velocity, m s^{-1}
x	Axial coordinate, m
Z	Mixture fraction
Z''^2	Mixture fraction variance
Greek Symbols	
α	Thermal diffusivity, m^2 s^{-1}
λ	Scaling parameter in Poisson equation
μ	Dynamic viscosity, kg m^{-1} s^{-1}
ρ	Density, kg m^{-3}
φ	Electric potential, V
ω	Relaxation factor in SOR method
Subscripts	
ref	Reference condition
i, j	Grid indices in r and z directions
in	Inlet condition
out	Outlet condition
n	Time level
n + 1	Next time level
Abbreviations	
CFD	Computational Fluid Dynamics
EHD	Electrohydrodynamics
FPV	Flamelet Progress Variable
PDF	Probability Density Function
SOR	Successive Over-Relaxation

References

1. Turns, S.R. *An Introduction to Combustion: Concepts and Applications*; McGraw-Hill: New York, NY, USA, 2012.
2. Lieuwen, T.; Yang, V. (Eds.) *Gas Turbine Emissions*; Cambridge University Press: Cambridge, UK, 2013.
3. Starikovskiy, A.; Aleksandrov, N. Plasma-assisted ignition and combustion. *Prog. Energy Combust. Sci.* **2013**, *39*, 61–110. [CrossRef]
4. Tropina, A.A.; Shneider, M.N.; Miles, R.B. Ignition by short duration, nonequilibrium plasma: Basic concepts and applications in internal combustion engines. *Combust. Sci. Technol.* **2016**, *188*, 831–852. [CrossRef]
5. Fialkov, A.B. Investigations on ions in flames. *Prog. Energy Combust. Sci.* **1997**, *23*, 399–528. [CrossRef]
6. Belhi, M.; Domingo, P.; Vervisch, P. Direct numerical simulation of the effect of an electric field on flame stability. *Combust. Flame* **2010**, *157*, 2286–2297. [CrossRef]
7. Ehn, A.; Petersson, P.; Zhu, J.J.; Li, Z.S.; Aldén, M.E.; Nilsson, E.J.; Larfeldt, J.; Larsson, A.; Hurtig, T.; Zettervall, N.; et al. Investigations of microwave stimulation of a turbulent low-swirl flame. *Proc. Combust. Inst.* **2017**, *36*, 4121–4128. [CrossRef]

8. Nordin-Bates, K.; Hurtig, T.; Zettervall, N.; Robertsson, R.; Nilsson, E.; Lörstad, D.; Ehn, A.; Fureby, C. Numerical simulation of microwave-enhanced low swirl methane-air flames. *Combust. Flame* **2026**, *285*, 114764. [CrossRef]
9. Gan, Y.; Luo, Y.; Wang, M.; Shi, Y.; Yan, Y. Effect of alternating electric fields on the behaviour of small-scale laminar diffusion flames. *Appl. Therm. Eng.* **2015**, *89*, 306–315. [CrossRef]
10. Jung, K.S.; Kim, S.O.; Lu, T.; Chung, S.H.; Lee, B.J.; Yoo, C.S. Differential diffusion effect on the stabilization characteristics of autoignited laminar lifted methane/hydrogen jet flames in heated coflow air. *Combust. Flame* **2018**, *198*, 305–319. [CrossRef]
11. Peters, N. Laminar diffusion flamelet models in non-premixed turbulent combustion. *Prog. Energy Combust. Sci.* **1984**, *10*, 319–339. [CrossRef]
12. Pierce, C.D.; Moin, P. Progress-variable approach for large-eddy simulation of non-premixed turbulent combustion. *J. Fluid Mech.* **2004**, *504*, 73–97. [CrossRef]
13. Ihme, M.; Pitsch, H. Prediction of extinction and reignition in nonpremixed turbulent flames using a flamelet/progress variable model. *Combust. Flame* **2008**, *155*, 90–107. [CrossRef]
14. Fiorina, B.; Gicquel, O.; Vervisch, L.; Carpentier, S.; Darabiha, N. Approximating the chemical structure of partially premixed and diffusion counterflow flames using FPI flamelet tabulation. *Combust. Flame* **2005**, *140*, 147–160. [CrossRef]
15. Domingo, P.; Vervisch, L.; Veynante, D. Large-eddy simulation of a lifted methane jet flame in a vitiated coflow. *Combust. Flame* **2008**, *152*, 415–432. [CrossRef]
16. Pecquery, F.; Moureau, V.; Lartigue, G.; Vervisch, L.; Roux, A. Modelling nitrogen oxide emissions in turbulent flames with air dilution: Application to LES of a non-premixed jet-flame. *Combust. Flame* **2014**, *161*, 496–509. [CrossRef]
17. Speelman, N.; de Goey, L.P.H.; van Oijen, J.A. Development of a numerical model for the electric current in burner-stabilised methane-air flames. *Combust. Theory Model.* **2015**, *19*, 159–187. [CrossRef]
18. Hu, J.; Rivin, B.; Sher, E. The effect of an electric field on the shape of co-flowing and candle-type methane-air flames. *Exp. Therm. Fluid Sci.* **2000**, *21*, 124–133. [CrossRef]
19. Yamashita, K.; Karnani, S.; Dunn-Rankin, D. Numerical prediction of ion current from a small methane jet flame. *Combust. Flame* **2009**, *156*, 1227–1233. [CrossRef]
20. Belhi, M.; Domingo, P.; Vervisch, P. Modelling of the effect of DC and AC electric fields on the stability of a lifted diffusion methane/air flame. *Combust. Theory Model.* **2013**, *17*, 749–787. [CrossRef]
21. Belhi, M.; Casey, T.A.; Han, J.; Bisetti, F.; Im, H.G.; Chen, J.Y. A computational study of the effects of AC electric fields on a laminar diffusion flame. *Proc. Combust. Inst.* **2015**, *35*, 3537–3545.
22. Di Renzo, M.; De Palma, P.; de Tullio, M.D.; Pascazio, G. An efficient flamelet progress-variable method for modeling non-premixed flames in weak electric fields. *J. Comput. Phys.* **2021**, *428*, 109963. [CrossRef]
23. Lacoste, D.A.; Moeck, J.P.; Roberts, W.L.; Chung, S.H.; Cha, M.S. Analysis of the step responses of laminar premixed flames to forcing by non-thermal plasma. *Proc. Combust. Inst.* **2017**, *36*, 4145–4153. [CrossRef]
24. Pilla, G.; Galley, D.; Lacoste, D.A.; Lacas, F.; Veynante, D.; Laux, C.O. Stabilization of a turbulent premixed flame using a nanosecond repetitively pulsed plasma. *IEEE Trans. Plasma Sci.* **2006**, *34*, 2471–2477. [CrossRef]
25. Semenov, E.S.; Sokolik, A.S. Thermal and chemical ionization in flames. *Combust. Explos. Shock Waves* **1970**, *6*, 33–43. [CrossRef]
26. Gillaspy, J.D. Highly charged ions. *J. Phys. B At. Mol. Opt. Phys.* **2001**, *34*, R93–R130. [CrossRef]
27. Popov, N.A. Kinetics of plasma-assisted combustion: Effect of non-equilibrium excitation on the ignition and oxidation of combustible mixtures. *Plasma Sources Sci. Technol.* **2016**, *25*, 043002. [CrossRef]
28. Ju, Y.; Sun, W. Plasma assisted combustion: Dynamics and chemistry. *Prog. Energy Combust. Sci.* **2015**, *48*, 21–83. [CrossRef]
29. Starikovskiy, A. Physics and chemistry of plasma-assisted combustion. *Philos. Trans. R. Soc. A Math. Phys. Eng. Sci.* **2015**, *373*, 20150074. [CrossRef]
30. Adamovich, I.V.; Lempert, W.R. Challenges in understanding and predictive model development of plasma-assisted combustion. *Plasma Phys. Control. Fusion* **2015**, *57*, 014001. [CrossRef]
31. Tsolas, N. Flow Reactor Studies of Non-Equilibrium Plasma Assisted Combustion Kinetics. Ph.D. Thesis, Pennsylvania State University, University Park, PA, USA, 2015.
32. Ju, Y.; Lefkowitz, J.K.; Reuter, C.B.; Won, S.H.; Yang, X.; Yang, S.; Sun, W.; Jiang, Z.; Chen, Q. Plasma assisted low temperature combustion. *Plasma Chem. Plasma Process.* **2016**, *36*, 85–105. [CrossRef]
33. Mahamud, R.; Tropina, A.A.; Shneider, M.N.; Miles, R.B. Dual-pulse laser ignition model. *Phys. Fluids* **2018**, *30*, 106104. [CrossRef]
34. Starikovskaia, S.; Lacoste, D.A.; Colonna, G. Non-equilibrium plasma for ignition and combustion enhancement. *Eur. Phys. J. D* **2021**, *75*, 231. [CrossRef]
35. Malé, Q.; Shcherbanev, S.; Noiray, N. Numerical study of plasma-assisted combustion in a sequential combustor. *Proc. Combust. Inst.* **2023**, *39*, 5447–5456. [CrossRef]
36. Guerra-Garcia, C.; Pavan, C.A. The backward problem in plasma-assisted combustion: Experiments of nanosecond pulsed discharges driven by flames. *Appl. Energy Combust. Sci.* **2023**, *15*, 100155. [CrossRef]

37. Perrin-Terrin, J.B.; Vaysse, N.; Durox, D.; Vicquelin, R.; Candel, S.; Laux, C.O.; Renaud, A. Plasma-assisted combustion of hydrogen swirling flames: Extension of lean blowout limit and NOx emissions. *Proc. Combust. Inst.* **2024**, *40*, 105546. [CrossRef]
38. Shejan, M.E.; Bhuiyan, S.M.Y.; Schoen, M.P.; Mahamud, R. Assessment of machine learning techniques for simulating reacting flow: From plasma-assisted ignition to turbulent flame propagation. *Energies* **2024**, *17*, 4887. [CrossRef]
39. Lin, P.T.; Shadid, J.N.; Tuminaro, R.S.; Sala, M.; Hennigan, G.L.; Pawlowski, R.P. A parallel fully coupled algebraic multilevel preconditioner applied to multiphysics PDE applications: Drift-diffusion, flow/transport/reaction, resistive MHD. *Int. J. Numer. Methods Fluids* **2010**, *64*, 1148–1179. [CrossRef]
40. Lele, S.K. Compact finite difference schemes with spectral-like resolution. *J. Comput. Phys.* **1992**, *103*, 16–42. [CrossRef]
41. Fu, D.; Ma, Y. A high order accurate difference scheme for complex flow fields. *J. Comput. Phys.* **1997**, *134*, 1–15. [CrossRef]
42. Fan, P. The standard upwind compact difference schemes for incompressible flow simulations. *J. Comput. Phys.* **2016**, *322*, 74–112. [CrossRef]
43. Mahamud, R.; Waters, J.; Bujack, R. A finite element method for compressible and turbulent multiphase flow instabilities with heat transfer. *Fluids* **2025**, *10*, 302. [CrossRef]
44. Dobbins, R.R.; Smooke, M.D. A fully implicit, compact finite difference method for the numerical solution of unsteady laminar flames. *Flow Turbul. Combust.* **2010**, *85*, 763–799. [CrossRef]
45. Biazar, J.; Mehrlatifan, M.B. A compact finite difference scheme for reaction-convection-diffusion equation. *Chiang Mai J. Sci.* **2018**, *45*, 1559–1568.
46. Haque, M.A.; Hasan, M.K.; Mahamud, R. A High-Order Compact Finite Difference Scheme for Flamelet-Based Scalar Transport in Non-Premixed Laminar Flames. *Phys. Fluids* **2024**, *37*, 083637. [CrossRef]
47. Mahamud, R.; Haque, M.A.; Hasan, M.K. Enhancing the fidelity of steady flamelet-based LES of turbulent non-premixed flames using high-order compact finite difference schemes. *AIP Adv.* **2026**, *16*, 025328. [CrossRef]
48. Lacoste, D.A.; Xu, D.A.; Moeck, J.P.; Laux, C.O. Dynamic response of a weakly turbulent lean-premixed flame to nanosecond repetitively pulsed discharges. *Proc. Combust. Inst.* **2013**, *34*, 3259–3266. [CrossRef]
49. Pavan, C.A.; Guerra-Garcia, C. Nanosecond pulsed discharge dynamics during passage of a transient laminar flame. *Plasma Sources Sci. Technol.* **2022**, *31*, 115016. [CrossRef]
50. Tropina, A.A.; Mahamud, R. Effect of plasma on the deflagration to detonation transition. *Combust. Sci. Technol.* **2022**, *194*, 2752–2770. [CrossRef]
51. Chen, B.S.; Garner, A.L.; Bane, S.P. Numerical analysis of a nanosecond repetitively pulsed plasma-assisted counterflow diffusion flame. *J. Appl. Phys.* **2023**, *133*, 203302. [CrossRef]
52. Wang, S.Q.; Darabiha, N.; Fiorina, B. Modeling turbulent flame enhancement by Nanosecond Repetitively Pulsed discharges using a low-order model. *Combust. Flame* **2026**, *285*, 114761. [CrossRef]
53. McEnally, C.S.; Pfefferle, L.D. Experimental study of nonfuel hydrocarbon concentrations in coflowing partially premixed methane/air flames. *Combust. Flame* **1999**, *118*, 619–632. [CrossRef]
54. Song, M.-Y.; Yoon, J.-S.; Cho, H.; Itikawa, Y.; Karwasz, G.P.; Kokoouline, V.; Nakamura, Y.; Tennyson, J. Cross sections for electron collisions with methane. *J. Phys. Chem. Ref. Data* **2015**, *44*, 023101. [CrossRef]
55. Tennyson, J.; Rahimi, S.; Hill, C.; Tse, L.; Vibhakar, A.; Akello-Egwel, D.; Brown, D.B.; Dzarasova, A.; Hamilton, J.R.; Jaksch, D. QDB: A new database of plasma chemistries and reactions. *Plasma Sources Sci. Technol.* **2017**, *26*, 055014. [CrossRef]
56. Tennyson, J.; Mohr, S.; Hanicinec, M.; Dzarasova, A.; Smith, C.; Waddington, S.; Liu, B.; Alves, L.L.; Bartschat, K.; Bogaerts, A. The 2021 release of the Quantemol database (QDB) of plasma chemistries and reactions. *Plasma Sources Sci. Technol.* **2022**, *31*, 095020. [CrossRef]
57. Smooke, M.D.; McEnally, C.S.; Pfefferle, L.D.; Hall, R.J.; Colket, M.B. Computational and experimental study of soot formation in a coflow, laminar diffusion flame. *Combust. Flame* **1999**, *117*, 117–139. [CrossRef]

Disclaimer/Publisher's Note: The statements, opinions and data contained in all publications are solely those of the individual author(s) and contributor(s) and not of MDPI and/or the editor(s). MDPI and/or the editor(s) disclaim responsibility for any injury to people or property resulting from any ideas, methods, instructions or products referred to in the content.